IEEE Open Journal of Antennas and Propagation

Received XX Month, XXXX; revised XX Month, XXXX; accepted XX Month, XXXX; Date of publication XX Month, XXXX; date of current version XX Month, XXXX.

Digital Object Identifier 10.1109/OJAP.2020.1234567

Design, Modeling, and Characterization of a Cascaded-Lens Antenna for 220 – 330 GHz with 51.1 dBi Gain

Joel Dittmer[1], Student Member, IEEE, Akanksha Bhutani[2], Senior Member, IEEE, Felix Beuthan[1], Jonas Krimmer[1], Thomas Zwick[2], Fellow, IEEE, Christian Koos[1], Sebastian Randel[1], Senior Member, IEEE

[1]Institute of Photonics and Quantum Electronics (IPQ), Karlsruhe Institute of Technology (KIT), Germany
[2]Institute of Radio Frequency Engineering and Electronics (IHE), Karlsruhe Institute of Technology (KIT), Germany

CORRESPONDING AUTHOR: Joel Dittmer (e-mail: joel.dittmer@kit.edu).

This work was financially supported by the Federal Ministry of Education and Research of Germany in the project "Open6GHub" (grant number: 16KISK010).

ABSTRACT

This paper presents a novel sub-THz high-gain cascaded-lens antenna design approach that employs Gaussian beam propagation combined with low-cost dielectric materials and standard manufacturing techniques. The proposed lens antenna, solely designed based on a Gaussian beam model, achieves a maximum measured peak gain of $51.1\,\mathrm{dBi}$ across a broad sub-THz frequency range from 220 to $330\,\mathrm{GHz}$, demonstrated for the first time, to the best of the authors' knowledge. The antenna comprises a WR3.4 diagonal horn as the primary radiator and a cascaded pair of dielectric lenses, comprising a double-concave lens followed by a double-convex lens. This cascaded configuration effectively controls beam divergence, increases the effective aperture, and enables higher gain with a more compact horn-to-lens spacing than conventional single-lens designs. An analytical model based on Gaussian-beam propagation is developed to predict the antenna's radiation characteristics, thereby reducing the need for time- and memory-intensive full-wave electromagnetic simulations in e.g., CST Microwave Studio Suite. The model's accuracy is validated through comparison with both simulations and measurements for a single-lens configuration at $240\,\mathrm{GHz}$, $280\,\mathrm{GHz}$, and $320\,\mathrm{GHz}$. The predicted results show excellent agreement with the measured radiation patterns and realized gain. For the cascaded-lens antenna, the theoretical and experimental peak-gain values agree closely across the entire operating band from 220 to $330\,\mathrm{GHz}$. The proposed cascaded-lens antenna features a compact form factor, a high gain-to-aperture ratio of $13.01\,\mathrm{mm}^{-2}$, a low sidelobe level of $-40\,\mathrm{dBc}$, and an aperture efficiency of 66%. These results highlight the cascaded-lens approach as an efficient and scalable solution for next-generation sub-THz high-gain antenna systems.

INDEX TERMS sub-THz, Antenna, Lens, High gain, Cascaded lens, Convex, Concave, WR3.4 antenna, Lens antenna, Gaussian, Quasi-optical, sub-THz communication.

I. Introduction

Sub-terahertz (sub-THz) point-to-point (P2P) communication is a promising technology for enabling high-data-rate wireless links in small-cell fronthaul networks spanning distances of a few hundred meters. Such links experience high free-space path loss (FSPL), which requires high antenna gain to extend the transmission distance for a given capacity and outage probability. To overcome this challenge, the equivalent isotropic radiated power (EIRP) must be maximized by increasing either the sub-THz signal source output power or the transmit antenna gain. However, increasing the transmitted power is constrained by two fundamental limitations. First, state-of-the-art sub-THz electronic and optoelectronic components, such as broadband

This work is licensed under a Creative Commons Attribution 4.0 License. For more information, see https://creativecommons.org/licenses/by/4.0/

photodiodes and monolithic microwave integrated circuits (MMICs), typically deliver an output power between $5\,\mathrm{dBm}$ to $15\,\mathrm{dBm}$ in the sub-THz regime [1]–[4]. Second, even the most advanced power-amplifier MMICs remain limited to a saturated output power of approximately $12\,\mathrm{dBm}$ [5]. On the receiver side, FSPL can partially be mitigated through low-noise receivers and amplifiers that offer high overall conversion gain, enhanced sensitivity, and wide dynamic range [6]–[8]. Nonetheless, as frequency increases, a trade-off emerges between achievable transmit output power, receiver sensitivity, and available bandwidth. A practical and cost-efficient method to improve the link budget is to increase the antenna gain of both the transmitter and receiver. Conventional implementations often result in bulky and impractical solutions, such as Cassegrain reflectors or large dielectric lens antennas [9], [10].

For the sub-THz range (i.e., $100\,\mathrm{GHz}$ to $1\,\mathrm{THz}$), Cassegrain reflectors and transmissive dielectric lens antennas have been demonstrated to achieve peak gains in the order of $30\,\mathrm{dBi}$ to $50\,\mathrm{dBi}$, with physical apertures spanning from a few millimeters up to $20\,\mathrm{cm}$ and beyond [9]–[22]. Although single-lens architectures are effective in achieving high gain, their suitability for compact or integrated systems is limited. Moreover, scaling such architectures to achieve aperture gains exceeding $50\,\mathrm{dBi}$ becomes increasingly impractical from both physical and computational perspectives.

This paper presents a novel sub-THz cascaded-lens antenna using low-cost dielectric materials and standard manufacturing techniques. The proposed lens antenna, solely designed based on a Gaussian beam model, achieves a measured peak gain of $51.1\,\mathrm{dBi}$ across a broad sub-THz range from 220 to $330\,\mathrm{GHz}$, demonstrated for the first time, to the best of the authors' knowledge. The antenna consists of a WR3.4 diagonal horn as the primary radiator and a cascaded pair of dielectric lenses, comprising a double-concave lens followed by a double-convex lens. This cascaded configuration effectively controls beam divergence, thereby increasing the effective aperture and enabling high gain with a more compact horn-to-lens spacing compared to conventional single-lens designs.

An analytical model based on Gaussian-beam propagation is developed to predict the antenna radiation characteristics, reducing the need for time- and memory-intensive full-wave electromagnetic simulations in e.g., CST Microwave Studio Suite. While Gaussian-beam propagation theory is well established, its systematic application and experimental validation for the design and optimization of a high-gain cascaded-lens antenna operating in the sub-THz frequency range represents the primary contribution of this work. The model's accuracy is validated through comparison with both simulations and measurements for a single-lens configuration at 240, 280, and $320\,\mathrm{GHz}$. The predicted results exhibit excellent agreement with measured radiation patterns and realized gain. For the cascaded-lens antenna, the theoretical and experimental peak gain values are found to match closely across the entire operating band of 220 to $330\,\mathrm{GHz}$.

The proposed cascaded-lens antenna demonstrates a compact form factor, a high gain-to-aperture ratio of $13.01\,\mathrm{mm}^{-2}$, a low sidelobe level of $-40\,\mathrm{dBc}$, and an aperture efficiency of 66%. These results highlight the cascaded-lens approach as an efficient and scalable solution for next-generation sub-THz high-gain antenna systems.

The paper is organized as follows. Section II presents an analytical antenna model based on a Gaussian-beam approximation, which describes the quasi-optical beam propagation in the proposed cascaded-lens antenna design. The analytical model is compared with full-wave electromagnetic (EM) simulation results of a WR3.4 diagonal horn with and without a single plano-convex dielectric lens. Section IV-A introduces the measurement setup used for far-field radiation pattern characterization, which validates the radiation characteristics predicted by the analytical model. Finally, Section IV-B presents antenna gain measurements of the single- and cascaded-lens antenna designs and compares the experimental results with both simulations and the analytical model based on the Gaussian-beam approximation.

II. Sub-THz Lens Antenna Design Methodology

In this work, a lens-antenna design methodology based on Gaussian-beam propagation is adopted to quickly estimate the radiation characteristics (i.e., directivity and full null beamwidth) of a lens antenna. The Gaussian-beam estimation results are compared with full-wave electromagnetic simulation results in Section III, as well as with the measurement results in Section IV of a primary radiator (i.e., a WR3.4 diagonal horn antenna followed by a convex lens antenna) thus validating that the Gaussian-beam design method is a fast and accurate approach for high-gain lens-antenna design in the sub-THz frequency range of 220 - $330\,\mathrm{GHz}$. The design method consists of three steps. First, an analytical characterization of the primary radiator is performed using Gaussian-beam theory to obtain the beam waist and Rayleigh length. Second, single- and cascaded-lens transformations are modeled using ray-transfer matrix theory and complex beam parameters to predict the evolution of beam divergence, wavefront curvature, and the resulting directivity. Finally, parameter optimization of lens focal lengths and inter-element distances is conducted to maximize the Rayleigh length at the system output, subject to practical constraints on spacing and lens size. This approach enables rapid estimation of achievable antenna directivity and guides the design of electrically large sub-THz lens apertures, for which full-wave simulation becomes computationally impractical.

A. Analytical Radiation Model

The theoretical analysis is based on the mathematical description of the radiation characteristics of the primary radiator, i.e., a WR3.4 diagonal horn antenna, using Gaussian-beam theory. Owing to its high gaussicity and rotational

symmetry, the horn radiation can be accurately approximated by a fundamental Gaussian mode. The transformation of the radiated beam by dielectric lenses is evaluated analytically using ray-transfer beam theory, enabling closed-form prediction of the Rayleigh length and far-field beam divergence. In such a point-to-point line-of-sight (LOS) wireless communication link, the received power depends on the transmitted power, the antenna gains, and the various propagation losses, including frequency- and distance-dependent free-space path loss. The relationship between the transmitted power P_{Tx} and the received power P_{Rx} in such an LOS link is expressed as

$$P_{\mathrm{Rx}} = \frac{P_{\mathrm{Tx}} G_{\mathrm{Tx}} G_{\mathrm{Rx}}}{\mathrm{FSPL} \cdot L_{\mathbf{e}}} \,. \tag{1}$$

Here, $G_{\mathbf{Tx}}$ and G_{Rx} denote the antenna gain at the transmitter (Tx) and receiver (Rx), respectively. FSPL represents the free-space path loss, while L_{e} accounts for additional link losses such as atmospheric absorption, misalignment, and polarization mismatch between the Tx and Rx antennas. The FSPL increases quadratically with both frequency f and transmission distance r and is expressed as [23]

$$\mathrm{FSPL} = \left(\frac{4\pi r f}{c}\right)^2 , \tag{2}$$

where c is the speed of light in vacuum.

At sub-THz frequencies, particularly around $300\,\mathrm{GHz}$, the high FSPL imposes significant constraints on link performance over long transmission distances. At a distance of $r = 100\,\mathrm{m}$, the FSPL is in the order of $122\,\mathrm{dB}$. To maintain sufficient received power, high-gain antennas must be employed at both the Tx and Rx to compensate for the high path loss. An effective method to enhance the directivity of a primary radiator at sub-THz frequencies, e.g., a standard horn antenna, is to employ a lens-based antenna system that further collimates the transmitted or received beam. However, the degrees of freedom, and hence the maximum achievable gain, are inherently limited in compact single-lens designs. To overcome this limitation, we introduce a novel cascaded-lens antenna consisting of a concave and a convex lens. This configuration provides additional control over the beam divergence and wavefront curvature of the sub-THz beam. A Gaussian-beam propagation model is adopted to efficiently estimate the cascaded-lens antenna directivity. This approach is advantageous, since full-wave EM simulations become increasingly impractical due to the large electrical size of high-gain aperture antennas. In this work, a WR3.4 diagonal horn antenna operating from $220\,\mathrm{GHz}$ to $330\,\mathrm{GHz}$ is employed as the primary radiator. The antenna exhibits high Gaussian beam purity [24], characterized by the Gaussicity η_{Gauss}, which is evaluated using the normalized overlap integral between the measured radiation pattern and an ideal Gaussian field distribution. This metric quantifies the degree to which the radiated field approximates an ideal Gaussian beam. The WR3.4 diagonal horn antenna exhibits a Gaussicity greater than 84% and a nearly rotationally symmetric far-field radiation pattern [25]. Therefore, the radiation pattern of the primary radiator is modeled using the Gaussian-beam approximation. The proposed Gaussian analytical model is first validated against both measured and simulated radiation characteristics of the primary radiator and a single-lens antenna. Because the cascaded-lens configuration exhibits an extremely high aperture gain exceeding $50\,\mathrm{dBi}$, neither direct far-field measurements using the setup described in Section IV nor full-wave EM simulations are feasible. Instead, the theoretical model is validated by comparing its predicted peak aperture gain with long-distance link measurements, demonstrating excellent agreement and confirming the accuracy of the Gaussian-beam-based approach. Applying the Gaussian approximation, the antenna's maximum directivity D_0, which is related to the full-width-at-half maximum (FWHM) angle in both the E- and H-plane, can simply be calculated by [26]

$$D_0 = \frac{4\pi}{\Theta_{\mathrm{FWHM,H}} \Theta_{\mathrm{FWHM,E}}} . \tag{3}$$

For a symmetric aperture that produces a rotationally symmetric Gaussian far-field radiation pattern, the FWHM beam-divergence angle is identical in both the E and H-planes, i.e., $\Theta_{\mathrm{FWHM}} = \Theta_{\mathrm{FWHM,H}} = \Theta_{\mathrm{FWHM,E}}$. Under these conditions, the FWHM divergence angle and the Rayleigh length of a Gaussian beam are analytically related as follows (see Appendix V-C for a detailed derivation)

$$\Theta_{\mathrm{FWHM}} = 2 \arctan\left(\sqrt{\frac{\ln(2)}{k z_{\mathrm{R}}}}\right) , \tag{4}$$

where $k = 2\pi/\lambda$ is the wavenumber with the free-space wavelength λ and z_{R} is the Rayleigh length of the Gaussian beam with

$$z_{\mathrm{R}} = \frac{\pi w_0^2}{\lambda} \,. \tag{5}$$

In the equation w_0 represents the beam waist radius. All aforementioned Gaussian-beam parameters are indicated in Fig. 1 for a horn antenna radiating a symmetric Gaussian-beam. For a narrow main lobe in the small-angle regime

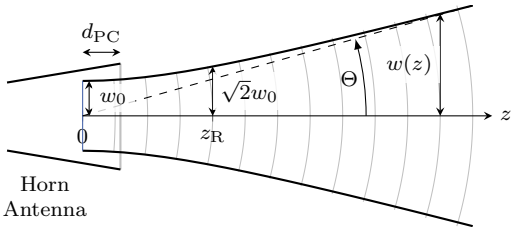

FIGURE 1. Schematic visualizing a Gaussian beam radiated from a horn antenna and the key parameters of the beam.

where $\arctan(x) \approx x$ and with rotational symmetry, this model yields a maximum far-field directivity of

$$D_0 \approx \frac{\pi k z_{\mathrm{R}}}{\ln(2)} \tag{6}$$

At an operating frequency of $280\,\mathrm{GHz}$ ($\lambda \approx 1.07\,\mathrm{mm}$) and a beam waist of $w_0 = 1.8\,\mathrm{mm}$, typical for a standard WR3.4

diagonal horn antenna, the Rayleigh length is $z_\mathrm{R} \approx 9.5\,\mathrm{mm}$. Using Eq. (4), the maximum directivity is approximately $24.25\,\mathrm{dBi}$, which agrees well with both theoretical predictions and full-wave simulations of sub-THz WR3.4 diagonal-horn antennas (see Section IV-B).

As indicated by Eqs. (4) and (6), the maximum directivity D_0 increases with the Rayleigh length z_R of the output Gaussian beam. Optimizing the Rayleigh length of the primary radiator with a single-convex (CX) lens allows for further collimation of the Gaussian beam emitted by the primary antenna. The Rayleigh length of the transformed beam $z_{\mathrm{R,CX}}$ after the collimating single-lens is given by (see Appendix V-B for the general derivation)

$$z_{\mathrm{R,CX}} = \frac{f_\mathrm{CX}^2 z_\mathrm{R}}{(f_\mathrm{CX}-d)^2 + z_\mathrm{R}^2} \quad \text{with} \quad z_{\mathrm{R,CX}}^{\max} = \frac{f_\mathrm{CX}^2}{z_\mathrm{R}}. \tag{7}$$

The maximum Rayleigh length occurs at $d = f_\mathrm{CX}$, yielding $z_{\mathrm{R,CX}}^{\max}$. Here, f_CX denotes the focal length of the convex lens and d is the distance between the horn antenna's phase center ($z = 0$), which is the origin of the Gaussian beam and the lens. By varying d, the Rayleigh length and consequently the directivity of the collimated beam changes for a fixed focal length f_CX. The aperture consisting of the horn antenna and the single convex lens is given in Fig. 2. For a collimating lens with a focal length of $f_\mathrm{CX} = 80\,\mathrm{mm}$,

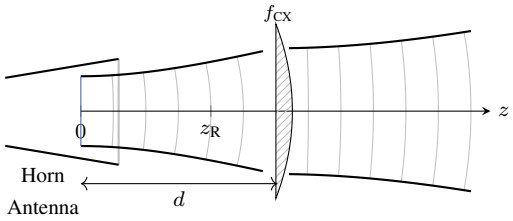

FIGURE 2. Gaussian beam parameters radiated by a horn antenna with single-convex lens.

the distance-dependent directivity is shown in Fig. 3. The maximum Rayleigh length is obtained at $d = f_\mathrm{CX}$, resulting in $z_{\mathrm{R,CX}}^{\max} = 0.67\,\mathrm{m}$, corresponding to a theoretical maximum directivity of approximately $D_0 \approx 42.5\,\mathrm{dBi}$. As indicated by

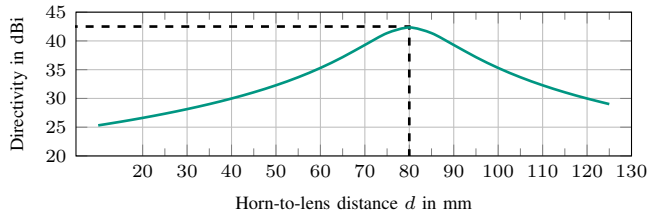

FIGURE 3. Distance dependent directivity for single-lens antenna.

Eq. (7), achieving an even high directivity of e.g., $54\,\mathrm{dBi}$, which is sufficient to compensate for the FSPL of a $25\,\mathrm{m}$ long link operating from 220 to 330 GHz, requires a horn-to-lens spacing of at least $30\,\mathrm{cm}$ with the corresponding focal length of $30\,\mathrm{cm}$.

B. Cascaded Lens Optimization

The achievable directivity of the lens antenna can be significantly enhanced by introducing a second lens element that provides additional control over the beam curvature and divergence. This allows for a significantly reduced overall horn-to-lens spacing, i.e., smaller overall dimensions in z-direction. The cascaded-lens antenna configuration, including the relative horn–lens and lens-to-lens spacings as well as the individual focal lengths, is shown in Fig. 4. For a cascaded concave–convex configuration, four parameters can be optimized to maximize the Rayleigh length at the system output, which directly determines the theoretical peak directivity. These parameters are the focal lengths of both lenses (f_CC and f_CX), the horn-to-lens distance (d), and the lens-to-lens spacing (d_LL). For a cascaded concave–convex

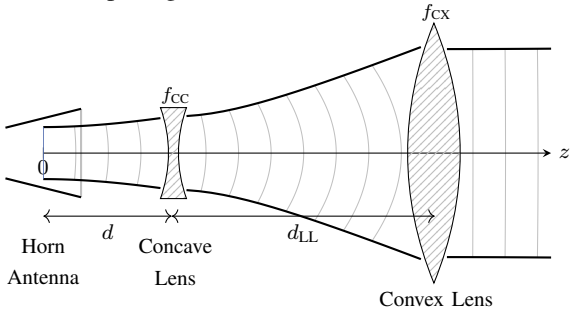

FIGURE 4. Gaussian beam radiated by a horn antenna with cascaded-lenses (double-concave and planar-convex lenses).

lens antenna, the resulting Rayleigh length of the Gaussian beam $z_{\mathrm{R,C}} = \mathrm{Im}\{\underline{q}_1\}$, can be calculated as described in Appendix V-B using the complex-valued beam parameter $\underline{q}_1$ to be

$$\underline{q}_1 = \frac{\left(1 - \frac{d_\mathrm{LL}}{f_\mathrm{CC}}\right)(d + \mathrm{j}z_\mathrm{R}) + d_\mathrm{LL}}{\left(\frac{d_\mathrm{LL}}{f_\mathrm{CC} f_\mathrm{CX}} - \frac{1}{f_\mathrm{CC}} - \frac{1}{f_\mathrm{CX}}\right)(d + \mathrm{j}z_\mathrm{R}) + 1 - \frac{d_\mathrm{LL}}{f_\mathrm{CX}}}. \tag{8}$$

Figure 4 illustrates the evolution of the Gaussian beam after passing through the concave and convex lenses. To achieve a directivity of up to $54\,\mathrm{dBi}$, the four key parameters are optimized. As shown in Fig. 5, each horn–to–concave-lens

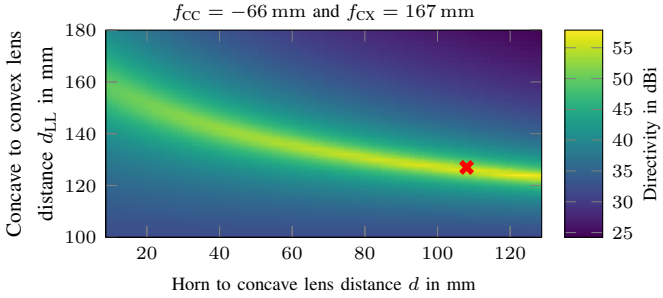

FIGURE 5. Directivity for cascaded-lens antenna. X indicates the used parameter combination for cascaded-lens measurements.

spacing d exhibits a distinct optimum concave–to–convex spacing d_LL that maximizes the cascaded-lens directivity. Increasing d allows the Gaussian beam to expand further before

entering the concave lens, enabling stronger recollimation by the convex lens and resulting in a higher directivity. However, this trend cannot be extended indefinitely. The maximum achievable directivity is ultimately constrained by several practical factors. First, the in-house CNC milling process enables arbitrary lens surface shaping but limits the maximum manufacturable lens diameter to $120\,\mathrm{mm}$. This constraint directly restricts the minimum feasible focal length to approximately $165\,\mathrm{mm}$, since achieving a shorter focal length would require a larger aperture diameter and a significantly thicker lens profile, both of which exceed fabrication capabilities and increase the losses in the lenses. Second, increasing the horn–to–lens and lens–to–lens distances beyond a certain point results in a physically long antenna structure, which becomes difficult to align in itself. Finally, spillover losses increase when lens diameters cannot fully contain the broadened beam at larger spacings. As a result, although the analytical model predicts monotonically increasing gain for increasing distances, practical lens diameter limits introduce an upper bound on the usable parameter space. For these reasons, the optimum parameter set indicated by "x" in Fig. 5 represents the highest directivity that can be achieved within realistic fabrication and alignment constraints. Considering the constraints imposed by the maximum feasible lens size, the smallest achievable lens antenna length, and the paraxial approximation, the optimized design, which is defined by $f_{\mathrm{CC}} = -66\,\mathrm{mm}$, $f_{\mathrm{CX}} = 167\,\mathrm{mm}$, $d = 108.3\,\mathrm{mm}$, and $d_{\mathrm{LL}} = 127.1\,\mathrm{mm}$, achieves a maximum directivity of $54.7\,\mathrm{dBi}$ based on the Gaussian-beam approximation (see Fig. 5). Notably, this performance is achieved with a total horn-to-lens spacing of $23.5\,\mathrm{cm}$, representing a substantial reduction compared to a single-lens antenna that would require approximately $30\,\mathrm{cm}$ horn-to-lens spacing. Table 1 compares the dimensions of the single- and cascaded-lens sub-THz antennas. The far-field radiation pattern in the symmetrical E- or H-plane for the horn antenna, the single-lens, and the cascaded-lens configurations can be calculated using the Gaussian intensity distribution. Within this model, the angular directivity profile $D(\varphi)$ is expressed as

TABLE 1. Dimensions of single- and cascaded-lens antenna achieving a directivity of 54.7 dBi.

	Single-lens ant.	Cascaded-lens ant.
Horn - lens distance	$d = 30\,\mathrm{cm}$	$d + d_{\mathrm{LL}} = 23.5\,\mathrm{cm}$
Lens diameter	$11.94\,\mathrm{cm}$	$14.54\,\mathrm{cm}$

$$D(\varphi) = D_0 \exp\left(-\frac{4\varphi^2 \ln(2)}{\Theta_{\mathrm{FWHM}}^2}\right), \tag{9}$$

where D_0 is the aforementioned peak directivity and Θ_{FWHM} is the full-width-at-half maximum of the main lobe. The factor $\ln(2)$ ensures that the intensity drops to half its maximum at $\varphi = \Theta_{\mathrm{FWHM}}/2$, consistent with the FWHM definition for a Gaussian-beam profile.

III. Full-Wave EM Simulation Verification

To validate the accuracy of the simplified Gaussian-beam model, full-wave electromagnetic (EM) simulations were performed using CST Microwave Studio Suite. The verification is divided into three parts corresponding to the primary radiator, the single-lens antenna, and the cascaded-lens antenna.

A. WR-3.4 Diagonal Horn Antenna

The WR-3.4 diagonal horn was simulated in CST Microwave Studio Suite to extract its far-field radiation pattern including both peak gain and directivity. The results serve as a baseline for validating the Gaussian-beam approximation of the primary radiator. The diagonal horn antenna was simulated using a hexahedral mesh with 12 cells per wavelength in the critical regions of the aperture and waveguide transition. This results in a total of $\approx 2.7 \times 10^8$ mesh cells. The metallic horn was modeled with finite conductivity to include ohmic losses. The excitation was applied as a fundamental TE_{10} waveguide mode at the WR-3.4 waveguide port. Far-field monitors were defined at $240\,\mathrm{GHz}$, $280\,\mathrm{GHz}$, and $320\,\mathrm{GHz}$, and open (add space) boundary conditions were applied in all radiating directions with a minimum distance of 2λ from the horn aperture. This configuration ensures accurate modeling of the near-field phase front and far-field directivity. The simulation model of the diagonal horn antenna is shown in Fig. 6a. The resulting angular directivity is given in Fig. 7. As shown in the figure, the analytical Gaussian model closely matches the CST-simulated main-lobe region, with slight deviation attributable to the finite gaussicity of the horn. This discrepancy is expected and becomes negligible once dielectric lens elements are introduced, as the field distribution becomes increasingly Gaussian-like.

B. Single-Lens Antenna

Full-wave EM simulations were also conducted for the single-lens antenna configuration. These simulations incorporate dielectric absorption, Fresnel reflections, and finite-aperture effects, providing a realistic reference for comparison with the analytical model. The single-lens antenna

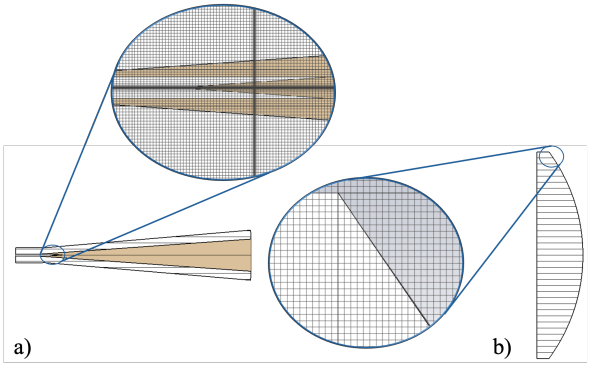

FIGURE 6. Simulation model of the horn antenna (a) and the single-lens antenna (a / b). Insets illustrate the mesh refinement in the WR3.4 diagonal horn antenna and on the lens surface, respectively.

was simulated using the same mesh refinement around the horn aperture, while the dielectric lens (PTFE, $\epsilon_r = 2.04$ and $\tan\delta = 0.001$ [27]) was assigned a mesh resolution of 12 cells per wavelength. This results in a total of $\approx 4.1 \times 10^9$ mesh cells. A plane-wave far-field monitor covering 220 GHz – 330 GHz was used. The horn–lens spacing was identical to the optimized analytical configuration to ensure a fair comparison. The simulation model for the single-lens antenna is shown in Fig. 6. The Gaussian-beam prediction exhibits excellent agreement with CST results (Fig. 7) for both the peak directivity and the angular directivity profile, validating the applicability of Gaussian optics for lens transformation at sub-THz frequencies.

C. Cascaded-Lens Antenna

Simulating the cascaded-lens antenna in CST results in a highly complex and computationally demanding model. The electrically large aperture, long propagation path, and multiple dielectric interfaces make accurate and time-efficient full-wave validation impractical for such high-gain sub-THz antennas. The full-wave simulation of the single-lens configuration already contained approximately $4.1 \cdot 10^9$ mesh cells. While this was still manageable, performing comparable simulations for the cascaded-lens antenna would have exceeded the computational capabilities of the available workstations. Consequently, only the Gaussian-beam model is presented for the cascaded-lens case in Fig. 7. This limitation highlights the key motivation for the proposed methodology, as relying exclusively on full-wave EM simulations to design and optimize high-gain lens antennas is computationally infeasible, making simplified analytical modeling both attractive and necessary.

Figure 7 summarizes the comparison between CST simulations and the Gaussian-beam model for the horn antenna, the single-lens antenna, and the analytically predicted cascaded-lens antenna. The calculated and simulated peak directivity values $D_0 = D(\varphi = 0)$ show close agreement across all configurations where full-wave simulations were feasible. The angular directivity profiles also align well within the main-lobe region, confirming the validity of the Gaussian-beam approach for predicting the radiation behavior of sub-THz lens antennas.

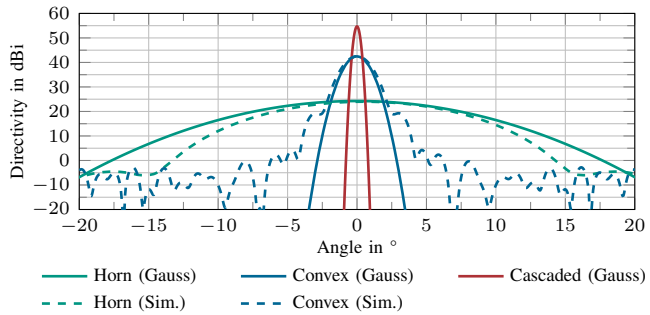

FIGURE 7. Gaussian model and simulated radiation pattern of horn antenna, single-lens antenna, and cascaded-lens antenna.

IV. Lens Antenna Measurement Setup

Based on the theoretical Gaussian model, which shows excellent agreement with full-wave simulations in CST Studio Suite, the lens antennas were fabricated using standard CNC milling. Two configurations were manufactured using Polytetrafluoroethylene (PTFE, commonly known as Teflon), which has a refractive index of $n_m = 1.46$:

1) A single-lens antenna utilizing a plano-convex lens with a focal length of $f_{\mathrm{CX}} = 80\,\mathrm{mm}$.
2) A cascaded-lens antenna composed of a double-concave lens ($f_{\mathrm{CC}} = -66\,\mathrm{mm}$) and a double-convex lens ($f_{\mathrm{CX}} = 167\,\mathrm{mm}$).

This manufacturing approach greatly reduces both cost and complexity compared with other state-of-the-art high-gain sub-THz lens antennas (Table 4). These alternative designs often rely on expensive silicon lenses, which necessitate both an anti-reflection coating for improved impedance matching to air and costly silicon micromachining processes. The radii of curvature (R_1 and R_2) of each PTFE lens surface were determined using the lensmaker's formula, as given below, prior to fabrication,

$$\frac{1}{f} = -\left(n_{\mathrm{m}} - 1\right)\left(\frac{1}{R_1} - \frac{1}{R_2}\right). \tag{10}$$

The measurement setup used to characterize antenna performance, specifically return loss, peak gain, and far-field radiation patterns, for the WR3.4 diagonal horn and single-lens antennas is shown in Fig. 8. A detailed description of this setup, which has been utilized for the characterization of antennas in the millimeter- and sub-millimeter-wave ranges, is provided in [28]–[30]. A concise overview is provided below to aid interpretation of the measured results for both the WR3.4 diagonal horn and single-lens antenna.

A vector network analyzer extension (VNAX) Tx/Rx module (Virginia Diodes, WR3.4 module) was connected to Port 1 of a millimeter-wave head controller (Keysight N5261A) and a PNA-X network analyzer (Keysight N5242B). The VNAX module up-converts the RF and LO signals generated by the PNA-X to the 220 - 330 GHz range and down-converts the reference and measurement IF signals back to baseband. The test port of the WR3.4 VNAX is connected to the antenna under test (AUT) via a short straight WR3.4 waveguide.

The peak gain and far-field radiation pattern of the AUT were measured using a WR3.4 standard-gain horn as the Rx antenna. The WR3.4 horn was connected to a compact Rx module (VDI WR3.4 MixAMC-I) comprising an integrated mixer–amplifier–multiplier chain [31]. The LO frequency range and multiplication factor of the Rx module were identical to those of the WR3.4 VNAX transmitter module. The down-converted IF signal and the required LO drive were routed to and from Port 2 of the PNA-X, respectively. The Rx module, consisting of the WR3.4 horn and WR3.4 MixAMC-I mixer, was mounted on a precision rotary arm aligned with the AUT boresight. The arm was rotated around

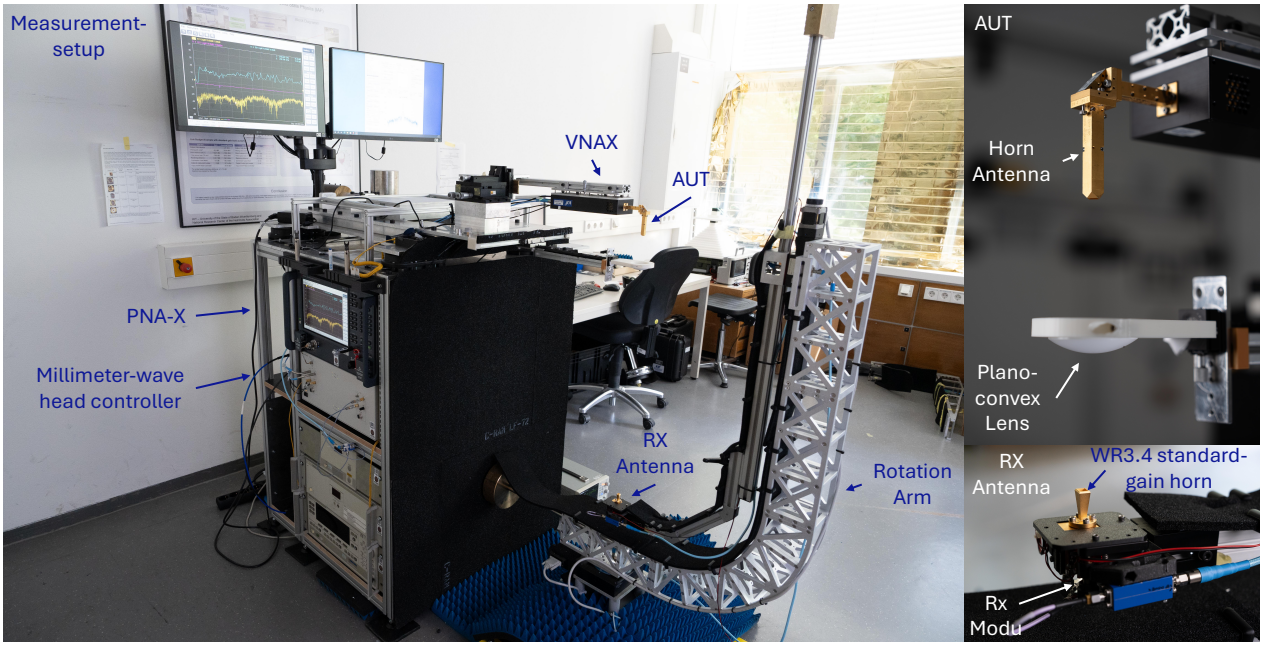

FIGURE 8. **Measurement setup used for the characterization of the WR3.4 diagonal horn and the single-lens antenna with a free-space distance** $70\,\mathrm{cm}$.

the AUT in precisely controlled angular steps to record the far-field radiation pattern.

A. Maximum Measurable Antenna Gain

The AUT, acting as the Tx antenna, was positioned at the rotation center of the receiving arm. The radial distance between the AUT (Tx), and the WR3.4 Rx horn antenna (Rx) is referred to as the far-field distance, denoted by R_{ff}. In this setup, R_{ff} is fixed at $70\,\mathrm{cm}$, limited by the physical dimensions of the measurement system. The far-field distance represents the region beyond which the spherical wavefront radiated by the AUT approximates a planar phase front characteristic of an ideal plane wave. For antennas with physical dimensions significantly larger than the free-space wavelength ($D >> \lambda$), e.g., horn antennas, the far-field distance is calculated using Eq. (11). This ensures that the radiated spherical wavefront deviates from an ideal plane wave by no more than 22.5° (or $\pi/8$ rad) in phase [32].

$$R_{\mathrm{ff}} \geq \frac{2D^2}{\lambda} \tag{11}$$

Over the $220\,\mathrm{GHz}$ to $330\,\mathrm{GHz}$ operating range, the corresponding free-space wavelength λ varies from $1.36\,\mathrm{mm}$ to $0.91\,\mathrm{mm}$. Substituting these wavelengths and a fixed far-field distance of $R_{\mathrm{ff}} = 70\,\mathrm{cm}$ into Eq. (11) gives a maximum permissible AUT diameter of $2.18\,\mathrm{cm}$ at $220\,\mathrm{GHz}$ and $1.78\,\mathrm{cm}$ at $330\,\mathrm{GHz}$. The corresponding maximum effective aperture area is $A_{\mathrm{e}} = D^2$. This aperture area is used to estimate the maximum theoretical antenna gain, assuming unity radiation efficiency, as given by Eq. (12) [33].

$$G_{\mathrm{max,\,AUT}} = \frac{4\pi}{\lambda^2} A_{\mathrm{e}} \tag{12}$$

Accordingly, the theoretical maximum gain is approximately $35\,\mathrm{dBi}$ at $220\,\mathrm{GHz}$ and $36.8\,\mathrm{dBi}$ at $330\,\mathrm{GHz}$. These values define the upper measurable gain limits for antennas radiating spherical wavefronts, constrained by the far-field condition of Eq. (11).

In a lens antenna, such as a WR3.4 diagonal horn combined with a single plano-convex lens, the horn serves as the primary radiator, while the lens, placed at a distance equal to its focal length, acts as the secondary radiator. The horn antenna emits a spherical wavefront, which is transformed into a planar wavefront by the lens [34]. Consequently, the far-field condition in Eq. (11) is no longer restrictive, since the lens antenna effectively radiates a planar wavefront. However, the radiated power from the lens AUT must remain below the 1-dB compression point of the Rx mixer (WR3.4 MixAMC-I). Therefore, the maximum antenna gain that can be measured for a lens AUT is constrained by the link budget of the measurement setup, as given in Eq. (13).

$$\begin{aligned} P_{\mathrm{out,\,VNAX}} + G_{\mathrm{max,\,Lens\text{-}AUT}} \\ - \mathrm{FSPL} + G_{\mathrm{Rx,\,Horn}} < P_{\mathrm{1dB,\,in,\,Rx}} \end{aligned} \tag{13}$$

In Eq. (13), $P_{\mathrm{out,\,VNAX}}$ represents the test port output power of the WR3.4 VNAX. $G_{\mathrm{max,\,Lens\text{-}AUT}}$ denotes the maximum gain of the lens AUT that can be measured using the setup shown in Fig. 8. FSPL refers to the free-space path loss over $70\,\mathrm{cm}$ Tx to Rx spacing, $G_{\mathrm{Rx,\,Horn}}$ is the gain of the WR3.4 standard gain horn on the Rx side, and $P_{\mathrm{1dB,\,in,\,Rx}}$ is the input RF power level at which the Rx mixer (WR3.4 MixAMC-I) enters $1\,\mathrm{dB}$ compression. The values of $P_{\mathrm{out,\,VNAX}}$, $G_{\mathrm{Rx,\,Horn}}$, and $P_{\mathrm{1dB,\,in,\,Rx}}$ were obtained from the respective component datasheets [35]–[37]. The FSPL was calculated from Eq. (2) using a $70\,\mathrm{cm}$ separation between the AUT and the Rx

horn. These values are substituted into Eq. (13) to determine $G_{\text{max, Lens-AUT}}$ and the results are summarized in Table 2 for the lower and upper bounds of the operating frequency range. As shown in Table 2, the maximum antenna gain that can be measured for a lens AUT using the setup illustrated in Fig. 8 is $42.2\,\text{dBi}$ at $220\,\text{GHz}$ and $42.7\,\text{dBi}$ at $330\,\text{GHz}$. Table IV-A summarizes the maximum measurable antenna gain at $220\,\text{GHz}$ and $330\,\text{GHz}$ for two types of AUTs. For a standard horn antenna, the measurement is limited by the far-field distance because it radiates a spherical wavefront. In contrast, for a lens antenna, the planar wavefront removes the far-field constraint, making the link-budget the limiting factor. As indicated by the analytical evaluation of the maximum measurable antenna gain, summarized in Table IV-A, only the radiation characteristics of the WR3.4 diagonal horn antenna and the single-lens antenna can be measured using the setup described above and shown in Fig. 8. To assess the peak gain performance ($G_0 = G(\varphi = 0, \vartheta = 0)$) of the cascaded-lens antenna, a modified measurement setup was used, employing the same VNAX at the Tx and the MixAMC-I at the Rx, with an increased free-space link distance of $5.1\,\text{m}$. The cascaded-lens antenna with Tx module is shown in Fig. 9. Increasing the link distance extends the dynamic range of the gain measurement setup, allowing for a maximum measurable lens antenna gain of $59.4\,\text{dBi}$ at $220\,\text{GHz}$ and $59.9\,\text{dBi}$ at $330\,\text{GHz}$ according to Eqs. 11 and 12.

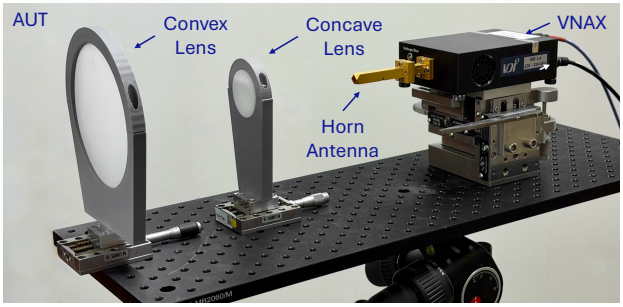

FIGURE 9. Experimental setup for characterizing the cascaded-lens antenna with a $5.1\,\text{m}$ free-space link. Only the transmitting (Tx) section and antenna under test (AUT) are shown. The receiving (Rx) side is identical to the configuration Fig. 8.

TABLE 2. Maximum measurable antenna gain of lens-AUT using the setup shown in Fig. 8.

Parameter	Value at $220\,\text{GHz}$	Value at $330\,\text{GHz}$
$P_{\text{out, VNAX}}$ [dBm]	1	1
$G_{\text{Rx, Horn}}$ [dBi]	23	26
λ [mm]	1.36	0.91
FSPL [dB]	76.2	79.7
$P_{\text{1dB,in,Rx}}$ [dBm]	-10	-10
$G_{\text{max, Lens-AUT}}$ [dBi]	42.2	42.7

The values of $G_{\text{max, Lens-AUT}}$ are calculated using Eq. (13). The values for $P_{\text{out, VNAX}}$, $G_{\text{Rx, Horn}}$, and $P_{\text{1dB,in,Rx}}$ are taken from manufacturer datasheets [35]–[37].

Antenna Type	$220\,\text{GHz}$ [dBi]	$330\,\text{GHz}$ [dBi]
Standard lens-AUT (Far-field limited)	< 35.0	< 36.8
Lens-AUT (Link-budget limited)	< 42.2	< 42.7

TABLE 3. Maximum measurable antenna gain for Standard and lens-AUT using setup shown in Fig. 8.

B. Measurement Results of the WR3.4 Diagonal-Horn, Single-, and Cascaded-Lens Antennas

The peak antenna gain G_0, predicted by the Gaussian-beam model (Section II) and defined as $G_0 = \eta' D_0$, is compared with the gain measured using the free-space measurement setup (Section IV-A) for three different systems. The WR3.4 diagonal horn and the single-lens antenna were measured using the $70\,\text{cm}$ measurement setup, shown in Fig. 8, while the higher-gain cascaded-lens antenna was measured using the $5.1\,\text{m}$ long setup, given in Fig. 9. The effective aperture efficiency η' is given by $\eta' = \eta\,\eta_{\text{Gauss}}$. Here, η represents dielectric and spillover losses, while η_{Gauss} accounts for the finite gaussicity of the primary radiator. Since the measurements for the gain of the WR3.4 diagonal horn do not include any lenses with dielectric losses, only the efficiency component related to limited gaussicity, $\eta' = \eta_{\text{Gauss}} = 84\%$, is considered in the calculation. The resulting radiation pattern and corresponding peak gain over frequency are shown in Fig. 10. As shown in the figure, the measurement, the full-wave simulation, and the Gaussian approximation agree closely, exhibiting similar peak gains and main-lobe radiation characteristics across the target frequency range from $220\,\text{GHz}$ to $330\,\text{GHz}$. Similarly, the single-lens antenna shows close agreement between the Gaussian model and the measured results across the target frequency range, as shown in Fig. 11. Taking the finite Gaussicity and the dielectric losses, associated with the

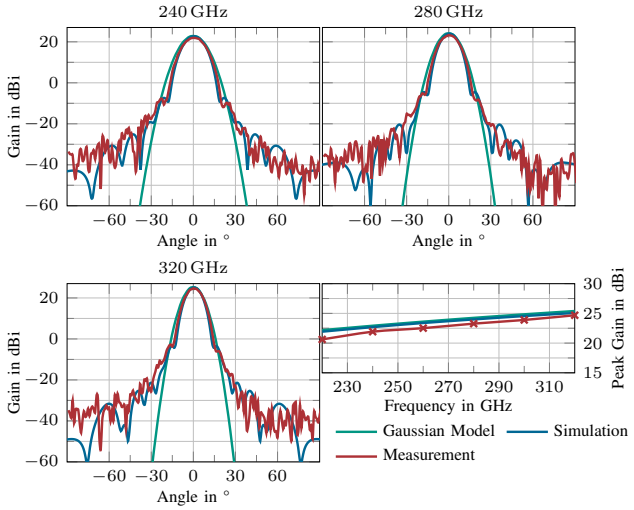

FIGURE 10. WR3.4 diagonal horn antenna: Gaussian model, simulated, and measured far-field radiation patterns at $240\,\text{GHz}$, $280\,\text{GHz}$, and $320\,\text{GHz}$, along with the peak antenna gain over the $220\,\text{GHz}$ to $330\,\text{GHz}$ range.

	Lens & Primary Radiator	Frequency Rel. Bandwidth	Lens Diameter Rel. Size	Peak Gain	Sidelobe level	Gain per Aperture	Sim. Rad. Efficiency
[11]	HDPE Lens & 20 dBi conical horn	220 - 330 GHz 40.7 %	140 mm 140λ	47 dBi	≈ -45 dBc	$3.26\,\mathrm{mm}^{-2}$	-2.8 dB
[22]	Silicon micromachined graded-index lens& 7.3 dBi open waveguide	500 - 750 GHz 40 %	12.18 mm 25.4λ	35.9 dBi	≈ -22 dBc	$33.4\,\mathrm{mm}^{-2}$	-0.5 dB
[13]	Silicon micromachined multi-beam graded-index & $2\times$7.3 dBi open waveguide	610 - 645 GHz 5.5 %	15.8 mm 33λ	32.1 dBi	≈ -23 dBc	$8.3\,\mathrm{mm}^{-2}$	-1.25 dB
[14]	Silicon micromachined graded-index lens & 7.3 dBi open waveguide	500 - 750 GHz 40 %	$\approx$7.9 mm 16.46λ	25.7 dBi	≈ -18 dBc	$7.6\,\mathrm{mm}^{-2}$	-0.85 dB
[15]	Silicon micromachined shallow lens & leaky waveguide feed	500 - 600 GHz 18.2 %	2.5 mm 4.58λ	23 dBi	≈ -20 dBc	$40.6\,\mathrm{mm}^{-2}$	-
[16]	Silicon micromachined lens & open waveguide	450 - 550 GHz 20 %	74 mm 123.3λ	50 dBi	≈ -25 dBc	$23.3\,\mathrm{mm}^{-2}$	-
[17]	Silicon micromachined gradient-index lens & corrugated horn	220 - 330 GHz 40.7 %	80 mm 68.7λ	$\approx$ 32 dBi*	-	$0.32\,\mathrm{mm}^{-2}$ *	-
[18]	Luneburg lens & planar antenna	220 - 290 GHz 27.5 %	10 mm 8.52λ	26.4 dBi	≈ -22 dBc	$5.56\,\mathrm{mm}^{-2}$	-6.99 dB
[20]	3D printed circularly polarized dielectric lens & 23 dBi LP horn	240 - 320 GHz 30.7 %	7.5 mm 6.5λ	31 dBi	≈ -28 dBc	$28.5\,\mathrm{mm}^{-2}$	-2.93 dB
[21]	Dielectric lens & open waveguide	230 - 310 GHz 29.6 %	20 mm 6.5λ	31.5 dBi	≈ -16 dBc	$18\,\mathrm{mm}^{-2}$	-
This work	**Concave & convex cascaded dielectric lenses & diagonal horn**	**220 - 330 GHz 40.7 %**	**112 mm 102λ**	**51.1 dBi**	< -40 **dBc**	**13.01** mm^{-2}	**-2.86 dB**

TABLE 4. Comparison with state-of-the-art high gain lens sub-THz antennas (* *Values calculated from data reported in cited papers*).

single lenses, an overall efficiency of $\eta' = \eta\,\eta_{\mathrm{Gauss}} \approx 65\%$ is evaluated trough full-wave simulations ($\eta \approx 78.5\%$) and the finite gaussicity of the primary radiator ($\eta_{\mathrm{Gauss}} = 84\%$). The simulations are discussed in detail in section III. Conversely, for the cascaded-lens antenna, a reduced total efficiency of $\eta' = \eta^2\,\eta_{\mathrm{Gauss}} \approx 52\%$ based on the single-lens simulation is considered, reflecting the expected increased dielectric losses due to the presence of an additional lens. These efficiencies represent aggregate estimates through simulations including dielectric absorption in PTFE (the dielectric constant and loss tangent at 300 GHz are $\epsilon_r = 2.04$ and $\tan\delta = 0.001$, respectively [27]), Fresnel reflections at lens surfaces, and spillover losses due to finite lens diameter. Additional losses caused by surface roughness are not considered in simulations. Based on the material loss tangent of PTFE the dominant contributions arise from dielectric absorption and interface reflections. For the cascaded-lens antenna, the peak gain was measured using the 5.1 m free-space link. Due to the increased electrical aperture size (exceeding 100λ), full-wave simulations using CST or similar tools were no longer computationally feasible (as discussed in Section II). Nevertheless, both the measurements and the Gaussian-beam model (shown in Fig. 12) consistently indicate a lens antenna gain ranging from 49 dBi to 51 dBi. The measured peak antenna efficiency according to [26], is given by

$$\eta_{\mathrm{ant.}} = \frac{A_{\mathrm{eff.}}}{A_{\mathrm{phys.}}} = \frac{G\lambda^2}{4\pi A_{\mathrm{phys.}}}\,, \tag{14}$$

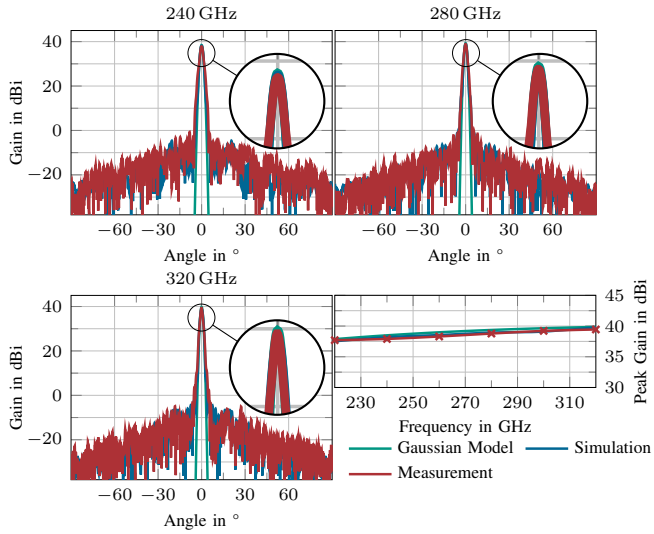

FIGURE 11. Single-lens antenna: Gaussian model, simulated, and measured far-field radiation patterns at 240 GHz, 280 GHz, and 320 GHz, along with the peak antenna gain over the 220 GHz to 330 GHz frequency range.

where G denotes the measured peak gain, λ is the wavelength, and $A_{\text{phys.}}$ represents the physical area of the lens. For the measured gain of the cascaded-lens antenna shown in Fig. 12, the resulting peak antenna efficiency is $\eta_{\text{ant.}} = 55\%$ to 66%, depending on the frequency. The extracted antenna efficiency of 55–66%, obtained from the measured peak gain (Eq. 14), is consistent with estimates based on the simulated efficiencies. Since the measured antenna efficiency is derived from the measured gain, it implicitly includes various loss mechanisms such as dielectric losses in the PTFE lens material, spillover loss due to the finite lens size, and impedance mismatch losses at both the primary radiator and the lens interfaces. The remaining mean absolute error between the measurement and the Gaussian-beam model shown in Fig. 12, which is $1.2\,\text{dB}$, is mainly attributed to systematic alignment errors between the Tx and Rx antennas over the $5.1\,\text{m}$ free-space link, as well as to residual uncertainty in the cascaded-lens efficiency. In the analytical Gaussian-beam model, the cascaded-lens efficiency is approximated as the product of the efficiencies of two identical single-lens stages, which represents a simplified assumption and does not fully capture additional loss mechanisms such as additional spillover losses and lens-to-lens interaction effects. The observed $0.3\,\text{dB}$ variations in the measured peak gain are attributed to calibration uncertainties of the VNAX power levels across the $220\,\text{GHz}$–$330\,\text{GHz}$ frequency range, as well as to measurement repeatability limits in the $5.1\,\text{m}$ free-space link.

Compared to previous demonstrations listed in Table 4, the proposed cascaded-lens antenna achieves the highest realized gain while maintaining one of the lowest sidelobe levels. This performance is achieved through low-cost fabrication using standard CNC milling with an inexpensive dielectric material, in contrast to the expensive silicon lenses that require both silicon micromachining and complex anti-reflection coatings.

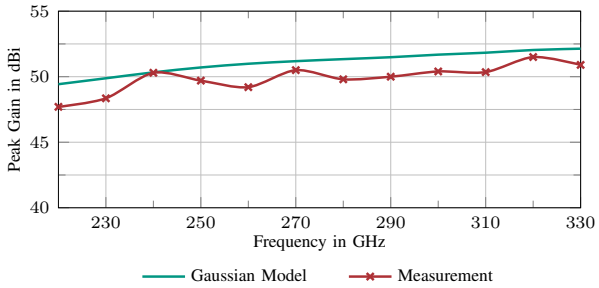

FIGURE 12. Cascaded-lens antenna: Gaussian model and measured far-field peak gain over the 220 GHz to 330 GHz frequency range.

V. Conclusion

In this paper, we present a novel cascaded-lens antenna design in which the beam radiated by a WR3.4 diagonal horn propagates through a cascade of a double-concave and a double-convex dielectric lens. The proposed cascaded-lens antenna controls the divergence of the beam radiated by the diagonal horn and thereby enabling high gain with a more compact horn-to-lens spacing.

An analytical model is developed to describe the quasi-optical beam propagation and to derive the antenna radiation characteristics. This model estimates the achievable directivity of a convex dielectric lens antenna for a set of parameters, including a lens focal length of $80\,\text{mm}$ and a horn-to-lens distance ranging from $10\,\text{mm}$ to $125\,\text{mm}$. The model is further extended to estimate the directivity of a cascaded-lens antenna with fixed focal lengths of $-66\,\text{mm}$ for the concave lens and $167\,\text{mm}$ for the convex lens, while varying the overall horn-to-lens and lens-to-lens distances. The analysis shows that the cascaded-lens antenna achieves a directivity of $54.7\,\text{dBi}$, a $12\,\text{dB}$ improvement over the single-lens design, at a shorter horn-to-lens distance than a single dielectric lens antenna arising from the increased degree of freedom, thereby offering a more compact solution for realizing high-gain sub-THz antennas.

The antenna radiation pattern predicted by the analytical model is compared with full-wave electromagnetic simulations of the WR3.4 diagonal horn and the single-lens antenna, showing very good agreement in terms of peak antenna gain. A sub-THz measurement setup is employed to measure the far-field radiation pattern of the WR3.4 diagonal horn and the single-lens antenna. The measured far-field radiation patterns are compared with both the Gaussian model and the simulation results at three frequencies, namely $240\,\text{GHz}$, $280\,\text{GHz}$, and $320\,\text{GHz}$. A good agreement is observed in all cases, with experimental peak gains of $21.9\,\text{dBi}$ ($240\,\text{GHz}$), $23.3\,\text{dBi}$ ($280\,\text{GHz}$), and $24.7\,\text{dBi}$ ($320\,\text{GHz}$) for the WR3.4 diagonal horn, and $37.9\,\text{dBi}$ ($240\,\text{GHz}$), $38.8\,\text{dBi}$ ($280\,\text{GHz}$), and $39.4\,\text{dBi}$ ($320\,\text{GHz}$) for the single-lens antenna.

A link budget analysis of the $70\,\text{cm}$ long far-field measurement setup shows that it can measure antennas with

a maximum gain of approximately $42\,\mathrm{dBi}$. Consequently, the cascaded-lens antenna gain was measured using a $5.1\,\mathrm{m}$ long free-space link. The measured peak antenna gain of the cascaded-lens antenna is compared with the Gaussian model across the $220\,\mathrm{GHz}$ to $330\,\mathrm{GHz}$ band, showing good agreement, with measured gain varying between $49\,\mathrm{dBi}$ and $51\,\mathrm{dBi}$ in the sub-THz range of interest. This confirms that the Gaussian beam model is a practical and accurate tool for the design of sub-THz high-gain antennas, offering rapid performance estimation and significant computational savings over full-wave methods.

In summary, when compared with other state-of-the-art high-gain sub-THz antennas (Table 4), the cascaded-lens antenna presented in this work demonstrates the highest realized peak antenna gain achieved over the largest reported sub-THz bandwidth of $220\,\mathrm{GHz}$ to $330\,\mathrm{GHz}$ (40% relative bandwidth). Moreover, among antennas achieving more than $50\,\mathrm{dBi}$ peak gain, the proposed design provides these gains with compact horn-to-lens spacing of $23.5\,\mathrm{cm}$, resulting in a higher gain per aperture of $13\,\mathrm{mm}^{-2}$ and a very low sidelobe level of $-40\,\mathrm{dBc}$. Furthermore, unlike most reported sub-THz lens antennas, which use costly materials (e.g., silicon lenses with matching layers) and expensive manufacturing techniques (e.g., silicon micromachining), the cascaded-lens antenna employs low-cost dielectric Teflon without the need for a matching layer and can be fabricated using standard CNC milling. Thus, the cascaded-lens antenna is a compact, high-directivity solution that can significantly enhance the link budget in sub-THz applications, including high-capacity wireless links and advanced sensing systems.

APPENDIX

A. Ray Transfer Matrix

A widely used method to describe optical or quasi-optical systems is through paraxial ray optics, often called ray transfer matrix analysis. This approach is valid under the assumption of infinitesimal wavelength and paraxial approximation, where all rays are assumed to remain close to the optical axis and at small angles Θ relative to it. At a given reference plane, a ray is characterized by its transverse displacement r from the optical axis and its inclination angle Θ. As the ray passes through an optical system, these quantities change according to the system's 2x2 ray transfer matrix $\boldsymbol{T}$. After traversing the system, the ray emerges with a new displacement r' and inclination Θ' given by the linear transformation [38]:

$$\begin{pmatrix} r' \\ \Theta' \end{pmatrix} = \underbrace{\begin{pmatrix} \mathfrak{a} & \mathfrak{b} \\ \mathfrak{c} & \mathfrak{d} \end{pmatrix}}_{\boldsymbol{T}} \cdot \begin{pmatrix} r \\ \Theta \end{pmatrix} .$$

For a thin lens with focal length f, the associated ray transfer matrix is given by

$$\boldsymbol{T}_{\text{lens}} = \begin{pmatrix} 1 & 0 \\ -\frac{1}{f} & 1 \end{pmatrix} .$$

Similarly, the ray transfer matrix for free-space propagation over a distance d is expressed as

$$\boldsymbol{T}_{\text{free-space}} = \begin{pmatrix} 1 & d \\ 0 & 1 \end{pmatrix} .$$

In general, the focal length f of a thin lens can be determined using the lens maker's equation as given in Eq. (10). According to the sign convention, the focal length f is positive for convex (converging) lenses and negative for concave (diverging) lenses.

B. Gaussian Beam

The Gaussian beam is a model that describes the transverse electric field profile of focused electromagnetic radiation. For a beam possessing rotational symmetry about its propagation axis, the spatial distribution is most conveniently described using cylindrical coordinates. In this system, the field's dependence on the transverse coordinates (x, y) is captured solely by the radial distance from the axis, $r = \sqrt{x^2 + y^2}$, and is expressed as [39], [40]

$$E\left(r, z\right) = E_0 \, \frac{w_0}{w\left(z\right)} \cdot \mathrm{e}^{-\frac{r^2}{w^2(z)}} \cdot \mathrm{e}^{-\mathrm{j}k\frac{r^2}{2R(z)}} \cdot \mathrm{e}^{-\mathrm{j}(kz - \zeta(z))} .$$

Here, $w(z)$ denotes the $1/\mathrm{e}$ beam radius and $R(z)$ the radius of curvature of the phase front at a distance z. These quantities are given by

$$w\left(z\right) = w_0 \sqrt{1 + \left(\frac{z}{z_{\mathrm{R}}}\right)^2} \quad \text{and} \quad R\left(z\right) = z\left(1 + \left(\frac{z_{\mathrm{R}}}{z}\right)^2\right),$$

where w_0 is the beam waist (the minimum beam radius at the focus, located at $z = 0$), and $z_{\mathrm{R}} = \frac{k w_0^2}{2}$ is the Rayleigh length, which defines the axial distance at which the beam radius increases by a factor of $\sqrt{2}$ compared to the radius at beam waist. The term $\zeta(z)$ represents the Gouy phase shift, an additional phase term that becomes significant near the beam waist. To simplify beam propagation analysis through optical systems, the Gaussian beam can be represented by a single complex-valued parameter known as the complex beam parameter

$$\frac{1}{\underline{q}\left(z\right)} = \frac{1}{R\left(z\right)} - \mathrm{j}\frac{2}{k w^2\left(z\right)} \quad \text{or} \quad \underline{q}\left(z\right) = z + \mathrm{j}z_{\mathrm{R}} .$$

This parameter compactly describes the beam curvature and width. The advantage of this parameter is that the system influence on the gaussian beam can still be evaluated based on the ray transfer matrix as for ray optical calculations [41]

$$\begin{pmatrix} \underline{q}_1 \\ 1 \end{pmatrix} = \alpha \begin{pmatrix} \mathfrak{a} & \mathfrak{b} \\ \mathfrak{c} & \mathfrak{d} \end{pmatrix} \cdot \begin{pmatrix} \underline{q}_0 \\ 1 \end{pmatrix}$$

resulting in

$$\underline{q}_1 = \frac{\mathfrak{a}\underline{q}_0 + \mathfrak{b}}{\mathfrak{c}\underline{q}_0 + \mathfrak{d}} .$$

This formulation facilitates efficient analysis of Gaussian beam propagation through cascaded optical and quasi-optical elements using ray-transfer matrices.

1) Single-Lens System

For the single-lens system, this results in

$$\boldsymbol{T}_{\text{system}} = \boldsymbol{T}_{\text{lens}} = \begin{pmatrix} 1 & 0 \\ -\frac{1}{f} & 1 \end{pmatrix}.$$

Resulting in the complex beam parameter

$$\underline{q}_1 = \frac{\underline{q}_0}{-\frac{\underline{q}_0}{f}+1} = \frac{\underline{q}_0 f}{f-\underline{q}_0} \overset{\underline{q}_0 = d + \mathrm{j}z_{\mathrm{R}}}{=} q_1 + \mathrm{j}\frac{f^2 z_{\mathrm{R}}}{(f-d)^2 + z_{\mathrm{R}}^2}$$

for a single-lens system with the distance between the lens and the focus point denoted as d and the focal length of the lens as f. q_1 represents the real part of $\underline{q}_1$, which is not required for further analysis.

2) Cascaded Lens System

For the cascaded-lens system, the ray transfer matrix is expressed as

$$\boldsymbol{T}_{\text{system}} = \underbrace{\begin{pmatrix} 1 & 0 \\ -\frac{1}{f_2} & 1 \end{pmatrix}}_{\text{2. Lens}} \cdot \underbrace{\begin{pmatrix} 1 & d_1 \\ 0 & 1 \end{pmatrix}}_{\text{Free-space}} \cdot \underbrace{\begin{pmatrix} 1 & 0 \\ -\frac{1}{f_1} & 1 \end{pmatrix}}_{\text{1. Lens}},$$

which is equal to

$$\boldsymbol{T}_{\text{system}} = \begin{pmatrix} 1-\frac{d_1}{f_1} & d_1 \\ \frac{d_1}{f_1 f_2} - \frac{1}{f_1} - \frac{1}{f_2} & 1-\frac{d_1}{f_2}. \end{pmatrix}.$$

The complex beam parameter $\underline{q}_1$ at the system output becomes

$$\underline{q}_1 = \frac{\left(1-\frac{d_1}{f_1}\right)\underline{q}_0 + d_1}{\left(\frac{d_1}{f_1 f_2} - \frac{1}{f_1} - \frac{1}{f_2}\right)\underline{q}_0 + 1 - \frac{d_1}{f_2}} = q_1 + \mathrm{j}z_{\mathrm{R},1},$$

where $z_{\mathrm{R},1} = \Im(\underline{q}_1)$ denotes the new Rayleigh length after the cascaded-lens system and q_1 represents the real part of $\underline{q}_1$, which is not required for further analysis.

C. Directivity for Gaussian Beam

To evaluate the directivity of a lensed antenna, the approximation given in [26] can be used:

$$D_0 = \frac{4\pi}{\Omega_{\mathrm{A}}},$$

where Ω_{A} is the beam solid angle. In the case of a narrow, symmetric main lobe, Ω_{A} can be estimated as the product of the angular beamwidths in the two principal orthogonal planes. Assuming the main lobe is approximately Gaussian and using the full-width at half-maximum (FWHM) angles in the E- and H-planes, we have

$$\Omega_{\mathrm{A}} \approx \Theta_{\mathrm{H}}\Theta_{\mathrm{E}},$$

where Θ_{H} and Θ_{E} denote the H- and E-FWHM beamwidths in radians. Note that for a symmetric beam $\Theta_{\mathrm{H}} = \Theta_{\mathrm{E}} = \Theta_{\mathrm{FWHM}}$. An expression for Θ_{FWHM} can be derived through the power distribution of a Gaussian beam, which is given by

$$P(r,z) \propto |E(r,z)|^2 = E_0^2 \frac{w_0^2}{w^2(z)} \cdot \mathrm{e}^{-2\frac{r^2}{w^2(z)}}.$$

The half-power beam width (HPBW) or full-width-at-half-maximum (FWHM) angle is defined as the angle at which the power of the beam in radial direction has decreased to half of the maximum power

$$P_{\max}(z) = P(0,z) \propto E_0^2 \frac{w_0^2}{w^2(z)}.$$

It can be achieved by first deriving the radius of half power r_{FWHM} according to

$$P(r_{\mathrm{FWHM}}, z) = \frac{1}{2} P_{\max}(z).$$

This results in

$$E_0^2 \frac{w_0^2}{w^2(z)} \cdot e^{-2\frac{r_{\mathrm{FWHM}}^2}{w^2(z)}} = \frac{1}{2} E_0^2 \frac{w_0^2}{w^2(z)}$$

and therefore

$$r_{\mathrm{FWHM}} = \sqrt{\frac{\ln 2}{2}} w(z).$$

From this, the two sided FWHM angle Θ_{FWHM} can be derived easily using trigonometric relations:

$$\Theta_{\mathrm{FWHM}} = 2\arctan\left(\frac{r_{\mathrm{FWHM}}}{z}\right) = 2\arctan\left(\sqrt{\frac{\ln 2}{2}}\frac{w(z)}{z}\right).$$

Far away from the antenna, i.e., for $z \gg z_{\mathrm{R}}$, the beam radius can be approximated by

$$w(z) = w_0\sqrt{1+\left(\frac{z}{z_{\mathrm{R}}}\right)^2} \approx \frac{w_0}{z_{\mathrm{R}}} z.$$

With $k = \frac{2\pi}{\lambda}$ and the expression for the FWHM angle this yields

$$\Theta_{\mathrm{FWHM}} = 2\arctan\left(\sqrt{\frac{\ln 2}{2}}\frac{w_0}{z_{\mathrm{R}}}\right) = 2\arctan\left(\sqrt{\frac{\ln(2)}{k\, z_{\mathrm{R}}}}\right).$$

For small angles ($\arctan(x) \approx x$) this results in

$$D_0 \approx \frac{4\pi}{\Theta_{\mathrm{FWHM}}^2} \approx \frac{\pi k z_{\mathrm{R}}}{\ln(2)}$$

Consequently, an increase in directivity, and thus in antenna gain, can be achieved by maximizing the imaginary part of the complex beam parameter $\underline{q}_1$, which corresponds to the Rayleigh length, at the output plane of the lens system.

Author Contribution

The conceptualization of this work was done by Joel Dittmer and Akanksha Bhutani. Measurements were conducted by Joel Dittmer, Felix Beuthan, and Akanksha Bhutani. Theoretical analysis was conducted by Joel Dittmer, Felix Beuthan, and Jonas Krimmer. The paper was written by Joel Dittmer and Akanksha Bhutani. Sebastian Randel, Christian Koos, Thomas Zwick, and Akanksha Bhutani acquired funding for this project. Overall supervision and coordination of this work was provided by Akanksha Bhutani and Sebastian Randel.

REFERENCES

[1] B. Schoch, A. Tessmann, A. Leuther, S. Wagner, and I. Kallfass, "260 GHz broadband power amplifier MMIC," *12th Germ. Microw. Conf. (GeMiC)*, 2019, pp. 232–235. doi: 10.23919/GEMIC.2019.8698140.

[2] Y.-s. Wu and J.-w. Shi, "Dynamic analysis of high-power and high-speed near-ballistic unitraveling carrier photodiodes at W-band," *IEEE Photon. Technol. Lett.*, vol. 20, no. 13, pp. 1160–1162, 2008. doi: 10.1109/lpt.2008.925195.

[3] J.-W. Shi *et al.*, "Extremely high saturation current-bandwidth product performance of a near-ballistic uni-traveling-carrier photodiode with a flip-chip bonding structure," *IEEE J. Quantum Electron.*, vol. 46, no. 1, pp. 80–86, 2009. doi: 10.1109/jqe.2009.2027339.

[4] M. Tonouchi, "Cutting-edge terahertz technology," *Nat. Photon.*, vol. 1, no. 2, pp. 97–105, 2007. doi: 10.1038/nphoton.2007.3.

[5] N. J. F. Buckwalter *et al.*, "Fundamental limits of high-efficiency silicon and compound semiconductor power amplifiers in 100–300 GHz bands," *ITU J. Future Evolving Technol.*, vol. 2, no. 7, pp. 39–50, 2021. doi: 10.52953/woxt4388.

[6] S. P. Singh, T. Rahkonen, M. E. Leinonen, and A. Parssinen, "A 290 GHz low noise amplifier operating above $f_{\max}/2$ in 130nm SiGe technology for sub-THz/THz receivers," *2021 IEEE Radio Freq. Integr. Circuits Symp. (RFIC)*, 2021, pp. 223–226. doi: 10.1109/rfic51843.2021.9490435.

[7] W. Feng, P. Yang, X. Sun, S. Liang, and Y. Zhang, "Development of 0.34 THz sub-harmonic mixer combining two-stage reduced matching technology with an improved active circuit model," *Appl. Sci.*, vol. 12, no. 24, p. 12855, 2022. doi: 10.3390/app122412855.

[8] I. Kallfass *et al.*, "Towards MMIC-based 300GHz indoor wireless communication systems," *IEICE Trans. Electron.*, vol. E98.C, no. 12, pp. 1081–1090, 2015. doi: 10.1587/transele.e98.c.1081.

[9] J.-N. Lee, K.-S. Kim, H. K. Kwon, and S.-B. Hyun, "Design and measurement method of small Cassegrain antenna for long-distance transmission," *2022 14th Global Symp. Millimeter-Waves Terahertz (GSMM)*, vol. 10, pp. 173–175, 2022. doi: 10.1109/gsmm53818.2022.9792327.

[10] Y. Wang, K. Zhu, Y. Xiao, H. Sun, and S. Li, "A Cassegrain antenna design for terahertz focal plane imaging system," *2021 Int. Appl. Comput. Electromagn. Soc. (ACES-China) Symp.*, 2021, pp. 1–2. doi: 10.23919/aces-china52398.2021.9581906.

[11] S. Nishi, K. Tamesue, T. Sato, S. H. Myint, T. Sato, and T. Kawanishi, "Design and evaluation of a lens horn antenna in the 300 GHz band," *2024 IEEE Int. Workshop Antenna Technol. (iWAT)*, 2024. doi: 10.1109/iwat57102.2024.10535865.

[12] I. Maestrojuan, V. Torres, and M. Goni, "Reflector and lens antennas for industrial applications in the sub-THz frequency spectrum," *2018 Asia-Pacific Microw. Conf. (APMC)*, 2018, pp. 37–39. doi: 10.23919/apmc.2018.8617434.

[13] A. Madannejad, M. M. Gohari, and J. Oberhammer, "Silicon-micromachined high-gain multi-beam beam-steering THz graded-index lens antenna enabled by a passive beamforming interposer," *19th Eur. Conf. Antennas Propag. (EuCAP)*, 2025, pp. 1–4. doi: 10.23919/eucap63536.2025.11000049.

[14] A. Madannejad, M. M. Gohari, U. Shah, and J. Oberhammer, "High-gain circularly polarized 500–750 GHz lens antenna enabled by silicon micromachining," *IEEE Trans. Antennas Propag.*, vol. 72, no. 5, pp. 4077–4085, 2024. doi: 10.1109/tap.2024.3383289.

[15] N. Llombart *et al.*, "Silicon micromachined lens antenna for THZ integrated heterodyne arrays," *IEEE Trans. Terahertz Sci. Technol.*, vol. 3, no. 5, pp. 515–523, 2013. doi: 10.1109/tthz.2013.2270300.

[16] S. Van Berkel, M. Alonso-delPino, C. Jung-Kubiak, and G. Chattopadhyay, "An $f/0.27$ high-gain lens antenna for ultrasmall platforms at THz frequencies," *IEEE Trans. Terahertz Sci. Technol.*, vol. 13, no. 5, pp. 549–560, 2023. doi: 10.1109/tthz.2023.3291450.

[17] F. Defrance *et al.*, "Flat silicon gradient index lens with deep reactive-ion-etched three-layer antireflection structure for millimeter and sub-millimeter wavelengths," *IEEE Trans. Terahertz Sci. Technol.*, vol. 15, no. 4, pp. 679-693, 2025. doi: 10.1109/TTHZ.2025.3555418.

[18] A. Mahmoud *et al.*, "Low-cost and low-profile sub-terahertz Luneburg lens beamformer on polymer," *IEEE Antennas Wireless Propag. Lett.*, vol. 22, no. 6, pp. 1411–1415, 2023. doi: 10.1109/lawp.2023.3243787.

[19] M. S. Li, R. T. Ako, S. Sriram, C. Fumeaux, and W. Withayachumnankul, "High-gain, low-profile, integrable planar lens antenna at 275 GHz," *2023 IEEE 11th Asia-Pacific Conf. Antennas Propag. (APCAP)*, 2023, pp. 1–2. doi: 10.1109/apcap59480.2023.10469730.

[20] G. B. Wu *et al.*, "High-gain circularly polarized lens antenna for terahertz applications," *IEEE Antennas Wireless Propag. Lett.*, vol. 18, no. 5, pp. 921–925, 2019. doi: 10.1109/lawp.2019.2905872.

[21] K. Konstantinidis *et al.*, "Low-THz dielectric lens antenna with integrated waveguide feed," *IEEE Trans. Terahertz Sci. Technol.*, vol. 7, no. 5, pp. 572–581, 2017. doi: 10.1109/tthz.2017.2725487.

[22] A. Madannejad, M. M. Gohari, U. Shah, and J. Oberhammer, "Graded index silicon micromachined lens antenna: Enabling 36-dBi gain and circular polarization at 500–750 GHz," *IEEE Trans. Antennas Propag.*, vol. 73, no. 8, pp. 6205–6210, 2025. doi: 10.1109/tap.2025.3567447.

[23] J. C. Whitaker *et al.*, *The Electronics Handbook*. Boca Raton, FL, USA: CRC Press, 2018.

[24] J. F. Johansson and N. D. Whyborn, "The diagonal horn as a sub-millimeter wave antenna," *IEEE Trans. Microw. Theory Techn.*, vol. 40, no. 5, pp. 795–800, 1992. doi: 10.1109/22.137380.

[25] V. Diodes, "Nominal horn specifications," 2020. [Online]. Available: https://www.vadiodes.com/images/AppNotes/VDI_Feedhorn_Summary_2020.05.04.pdf. [Accessed: Dec. 10, 2025].

[26] C. A. Balanis, *Antenna Theory Analysis and Design*, 3rd ed. Hoboken, NJ, USA: Wiley-Interscience, 2005.

[27] B. Stöckel, "Quasi-optical measurement of complex dielectric constant at 300 GHz," *Int. J. Infrared Millimeter Waves*, vol. 14, no. 10, pp. 2131–2148, 1993. doi: 10.1007/bf02096378.

[28] S. Beer and T. Zwick, "Probe based radiation pattern measurements for highly integrated millimeter-wave antennas," *Proc. 4th Eur. Conf. Antennas Propag. (EuCAP)*, 2010, pp. 1–5.

[29] H. Gulan *et al.*, "Probe based antenna measurements up to 325 GHz for upcoming millimeter-wave applications," *Proc. Int. Workshop Antenna Technol. (iWAT)*, 2013. doi: 10.1109/iwat.2013.6518338.

[30] M. Kretschmann, T. Zwick, and A. Bhutani, "Antenna measurement setup in the WM-570 and WM-380 frequency band," *IEEE Trans. Terahertz Sci. Technol.*, vol. 15, no. 6, pp. 951–962, 2025. doi: 10.1109/tthz.2025.3564771.

[31] Virginia Diodes, Inc., *Integrated Mixer/Amplifier/Multiplier Chain (MixAMC-I) Operational Manual*, Rev. 2024.09.22, 2024. [Online]. Available: https://www.vadiodes.com/images/Products/Int-AMC_MixAMC/RESOURCES/VDI-741_MixAMC-I_Product_Manual.pdf. [Accessed: Dec. 10, 2025].

[32] C. A. Balanis, "Linear wire antennas," *Antenna Theory: Analysis and Design*, 3rd ed. Hoboken, NJ, USA: John Wiley & Sons, Inc., 2016, ch. 4, pp. 151–219.

[33] C. A. Balanis, "Fundamental parameters of antennas," *Antenna Theory: Analysis and Design*, 3rd ed. Hoboken, NJ, USA: John Wiley & Sons, Inc., 2016, ch. 2, pp. 27–114.

[34] C. A. Fernandes, E. B. Lima, and J. R. Costa, "Dielectric lens antennas," *Handbook of Antenna Technologies*, Z. N. Chen, Ed. Singapore: Springer, 2016, pp. 1001–1064. doi: 10.1007/978-981-4560-44-3_40.

[35] Virginia Diodes, Inc., *Summary of Performance Specifications VNA Frequency Extension Modules*, VDI-956 Rev. 2024.09.18, 2024. [Online]. Available: https://www.vadiodes.com/images/Products/VNA/Specs_Sheets/VDI-956_VNA-X_Typical_Performance.pdf. [Accessed: Dec. 10, 2025].

[36] Virginia Diodes, Inc., *VDI Integrated Mixer / Amplifier / Multiplier Chain Specifications*, Rev. 2024.03.08, 2024. [Online]. Available: https://www.vadiodes.com/images/Products/Int-AMC_MixAMC/RESOURCES/VDI_iMixAMC_Specifications_2024.03.08.pdf. [Accessed: Dec. 10, 2025].

[37] MI-WAVE Millimeter Wave Products, Inc., *WR-3 Standard Gain Horn Antennas, 261J-25/387*, 2024. [Online]. Available: https://www.miwv.com/wp-content/uploads/2024/04/261J-25dB-Pattern.pdf. [Accessed: Dec. 10, 2025].

[38] E. Hecht, *Optics*, Global Ed. New York, NY, USA: Pearson, 2016.

[39] J. T. Verdeyen, *Laser Electronics*. Englewood Cliffs, NJ, USA: Prentice Hall, 1989.

[40] J. W. Goodman, *Introduction to Fourier Optics*. New York, NY, USA: McGraw-Hill, 1996.

[41] C. O'Sullivan and J. A. Murphy, *Field Guide to Terahertz Sources, Detectors, and Optics*. Bellingham, WA, USA: SPIE Press, 2012.

Joel Dittmer was born in Karlsruhe, Germany, in 1995. He received the B.Sc. and M.Sc. degrees in electrical engineering from the Karlsruhe Institute of Technology, Karlsruhe, Germany, in 2020 and 2022, respectively. He joined the Institute of Photonics and Quantum Electronics (IPQ) at the Karlsruhe Institute of Technology in 2023, where he started as a research assistant in the field of optoelectronic and electronic generated Terahertz signals for wireless communications. His research interests include THz system design, THz package design, and high data rate digital signal processing.

Akanksha Bhutani earned her M.Sc. and Ph.D. in Electrical Engineering and Information Technology from the Karlsruhe Institute of Technology (KIT), Germany, in 2012 and 2019, respectively. Since 2019, she has been leading the Antennas and Packaging research group at KIT's Institute of Radio Frequency Engineering and Electronics. Her work focuses on THz antennas and packaging for radar and wireless communication. Bhutani's accolades include the "Carl Freundenberg Prize" and the "Südwestmetall Advancement Award" for her dissertation in 2019 and 2020, the IEEE Microwave Magazine Best Paper Award in 2017, and the European Microwave Week (EuMW) Best Paper Awards in 2019 and 2022 and the International IHP "Wolfgang Mehr" Fellowship Award by the Leibniz-Institut für innovative Mikroelektronik (IHP) in 2023. In 2023, she served as the Operations Officer of EuMW 2023 held in Berlin. She has authored and co-authored over 50 research papers.

Felix Beuthan is currently pursuing his master's degree in electrical engineering at the Institute of Photonics and Quantum Electronics at the Karlsruhe Institute of Technology. He is currently working as a research assistant with his focus on terahertz communication technologies. His research interests and experiences include optical communication systems, terahertz technologies and their applications in advanced communication networks.

Jonas Krimmer earned his B.Sc. and M.Sc. degrees in electrical engineering from the Karlsruhe Institute of Technology (KIT) in Karlsruhe, Germany, in 2017 and 2020, respectively. In 2020, he joined the Institute of Photonics and Quantum Electronics (IPQ) at KIT, where he is currently pursuing his Ph.D. His research interests include free-space optical communications, space-division multiplexing, and digital signal processing for optical communications.

Thomas Zwick (Fellow, IEEE) received the Dipl.-Ing. (M.S.E.E.) and the Dr.-Ing. (Ph.D.E.E.) degrees from the University Karlsruhe (TH), Germany, in 1994 and 1999, respectively. From 1994 to 2001 he was a research assistant at the Institut für Hochstfrequenztechnik und Elektronik (IHE) at the University Karlsruhe (TH), Germany. In February 2001 he joined IBM as research staff member at the IBM T. J. Watson Research Center, Yorktown Heights, NY, USA. From October 2004 to September 2007, Thomas Zwick was with Siemens AG, Lindau, Germany. During this period he managed the RF development team for automotive radars. In October 2007, he became a full professor at the Karlsruhe Institute of Technology (KIT), Germany. He is the director of the Institut für Hochfrequenztechnik und Elektronik (IHE) at the KIT.

Christian Koos received the Ph.D. (Dr.-Ing.) degree in electrical engineering from the University of Karlsruhe, Karlsruhe, Germany, in 2007. He is currently a full Professor with the Karlsruhe Institute of Technology, Karlsruhe, Germany, where he is heading the Institute of Photonics and Quantum Electronics. He has co-founded several start-up companies, such as Vanguard Photonics GmbH, Vanguard Automation GmbH, SilOriX GmbH, and DeepLight SA. From 2008 to 2010, he was affiliated with the Corporate Research and Technology Department of Carl Zeiss AG in Oberkochen, Germany, where he led the technology forecast in the area of nanotechnology. He is the author of more than 140 journal papers and more than 30 patent families. His research interests include silicon photonics and hybrid integration concepts along with the associated applications in high-speed communications, optical sensing and metrology, and ultra-fast photonic-electronic signal processing. He was the recipient of several research awards and prestigious grants, such as the ERC Starting Grant in 2011 and ERC Consolidator Grant in 2017.

Sebastian Randel (Senior Member, IEEE) received the Dr.-Ing. degree for his work on high-speed optical-time-division-multiplexed transmission systems from Technische Universität Berlin, Berlin, Germany, in 2005. He is currently a full Professor with the Karlsruhe Institute of Technology, Karlsruhe, Germany, where he is co-heading the Institute of Photonics and Quantum Electronics. From 2005 to 2010, he was a Research Scientist with Siemens Corporate Technology, Munich, Germany, where he led research and standardization activities in the fields of polymer-optical-fiber communications, visible-light communications, and optical access networks. From 2010 to 2016, he was a Member of Technical Staff with Bell Laboratories, Holmdel, NJ, USA. His current research focuses on high-capacity power-efficient optical and sub-THz communication systems and networks.